physchem

MDPI

Article

Deciphering the Molecular Mechanism of Intramolecular Reactions from the Perspective of Bonding Evolution Theory

Abel Idrice Adjieufack [1,2,3,*], Juan Andrés [4], Mónica Oliva [4] and Vicent Sixte Safont [4,*]

1 Laboratory of Theoretical Chemistry (LCT), Namur Institute of Structured Matter (NISM), University of Namur, Rue de Bruxelles, 61, B-5000 Namur, Belgium
2 Physical and Theoretical Chemistry Laboratory, University of Yaoundé 1, Yaoundé P.O. Box 812, Cameroon
3 Computational Chemistry Laboratory, High Teacher Training College, University of Yaoundé 1, Yaoundé P.O. Box 47, Cameroon
4 Departament de Química Física i Analítica, Universitat Jaume I, Avda, Sos Baynat s/n, 12071 Castelló, Spain; andres@uji.es (J.A.); oliva@uji.es (M.O.)
* Correspondence: adjieufack21@gmail.com (A.I.A.); safont@uji.es (V.S.S.)

Abstract: The molecular mechanisms of three intramolecular rearrangements (I, the rearrangement of allyloxycycloheptatriene to yield tricyclic ketones; II, the cycloaddition of a nitrone-alkene to render two tricyclic isoxazolidines; and III, the decomposition of N-carbamoyl-L-proline in tetrahydro-1*H*-pyrrolo[1,2-*c*]imidazole-1,3(2*H*)-dione plus water, or tetrahydro-1*H*,3*H*-pyrrolo[1,2-*c*]oxazole-1,3-dione plus ammonia) have been studied by means of the bonding evolution theory (BET). The thermal rearrangement I is composed by a sigmatropic rearrangement coupled to an intramolecular Diels–Alder reaction. The sigmatropic reaction comprises four steps: (1) rupture of an O-C single chemical bond, (2) transformation of a C-O single to double bond, (3) creation of pseudo-radical centers on carbon atoms coupled with a double C-C bond evolving to single and the other C-C double bond migration, and (4) formation of the new C-C single bond. For the Diels–Alder reaction, the process can be described as an initial formation of up to four monosynaptic V(C) basins in two successive steps, coupled with the loss of the double bond character of the three initial double bonds, followed by the consecutive formation of two new C-C bonds, with the new double C-C bond formation sensed in between the formation of the first and the second C-C bonds. For reaction II, the bond forming process is described by the depopulation of N-C and C-C double bonds with the creation of a V(N) and two V(C) monosynaptic basins, followed by an O-C and C-C bond-forming processes via the creation of V(O,C) and V(C,C) disynaptic basins. Finally, for the thermal decomposition III, the reaction mechanism for the water elimination takes place in four events which can be summarized as follows: (1) the depopulation of V(N) with the formation of C-N, (2) the rupture of the C-O bond with transfer of its population to V(O), (3) the restoration of an N nitrogen lone pair via H-N bond cleavage, and (4) the formation of O-H illustrating the water molecule release. For the case of deamination, the events (1) and (2) correspond to the breaking and forming process of H-O and H-N bonds, respectively, while last events deal with the C-O bond formation and the elimination of the NH_3 molecule.

Keywords: bonding evolution theory (BET); electron localization function (ELF); catastrophe theory; intramolecular reactions

check for updates

Citation: Adjieufack, A.I.; Andrés, J.; Oliva, M.; Safont, V.S. Deciphering the Molecular Mechanism of Intramolecular Reactions from the Perspective of Bonding Evolution Theory. *Physchem* **2022**, *2*, 207–223. https://doi.org/10.3390/physchem2030015

Academic Editor: Jacinto Sá

Received: 28 March 2022
Accepted: 28 May 2022
Published: 28 June 2022

Publisher's Note: MDPI stays neutral with regard to jurisdictional claims in published maps and institutional affiliations.

Copyright: © 2022 by the authors. Licensee MDPI, Basel, Switzerland. This article is an open access article distributed under the terms and conditions of the Creative Commons Attribution (CC BY) license (https://creativecommons.org/licenses/by/4.0/).

1. Introduction

The concept of bonding is central to understanding chemical structures and reactions [1,2]. Chemical rearrangements involve the formation or cleavage of chemical bonds when they take place. However, the criteria used for characterizing a chemical bond, its physical origin and nature are still a subject of debate.

The foundation of chemical bonding was laid with the "electronic structure revolution" initiated by Gilbert Lewis, in which the fundamental concept of the chemical bond as a pair

of shared electrons between two or more nuclei was established [3]. During several decades, Lewis's idea was a cornerstone for many quantum theories such as valence bond (VB) theory [4,5], molecular orbital (MO) theory [6] and conceptual density functional theory (CDFT) [7,8] that have been developed for the understanding of the structure of matter and chemical reactivity. However, the main question related to how the chemical bond forming and breaking process takes place along the reaction pathway remains a big challenge for organic chemists. From the electron density, which is experimentally measurable (X-ray diffraction spectra), Bader has shown that it is possible to rigorously divide the molecular space in atomic volumes within his quantum theory called "Quantum Theory of Atoms in Molecules" (QTAIM) [9,10]. QTAIM is a quantum model that characterizes the chemical bond of a molecular system via a topological charge density approach. QTAIM also allows determination of certain physical properties such as atomic charges, energy and electric multipoles [10]. In addition, QTAIM was the cornerstone for the development of Quantum Chemical Topology, which has been related to Electron Localization Function (ELF) proposed by Becke and Edgecombe [11] and Electron Localizability Indicator (ELI-D) proposed by Kohout [12,13]. ELF measures the probability to find an electron pair in a multi-electron system while ELI-D carries out the chemical bonding signatures in a molecular system.

The development of the ELF and ELI-D functions has allowed the study of electron density rearrangement of bonding changes along a reaction path to become an attractive method to characterize a reaction mechanism. To perform these analyses quantitatively, Krokidis and Silvi proposed the joint use of ELF topology [11] and Thom's catastrophe theory (CT) [14] within the Bonding Evolution Theory, BET [15,16] as a new tool for studying the electronic changes occurring along a given chemical rearrangement. BET has been used as an appropriate quantum tool to gain a deep insight into the molecular mechanisms on a wide range of chemical reactions including denitrogenations, decompositions, formation of anionic complexes, cycloadditions [17–32] and even radical reactions [33].

In this work, we will continue this research line by studying the changes of electron density associated with the different reaction pathways of three intramolecular reactions. The first one we will investigate is the rearrangement of allyloxycycloheptatriene to yield tricyclic ketones, that was studied by Cupas et al. [34], who performed a chemical thermal rearrangement of allyloxycycloheptatriene in order to prepare new bridged polycyclic hydrocarbon derivatives (tricyclic ketones) via [3,3] sigmatropic and intramolecular Diels–Alder reactions. The second example was taken from the work of Saubern et al. [35], in which the synthesis of tricyclic-isoxazolidine molecules via intramolecular [3 + 2] cycloaddition reactions of nitrones is reported, while the associated potential energy surfaces have been explored by Chafaa et al. [36]. Both studies concluded that the fused/endo was the most favorable reaction path among fused and bridged reaction paths. The third and final example was extracted from the Seijas et al. paper [37]. They studied the conversion of N-carbamoyl-L-proline into hydantoin-L-proline using powder synchrotron X-ray diffraction and by direct heating at 470 K. The authors proposed a reaction mechanism (nucleophilic intramolecular substitution) involving both the lone pair of the NH_2 group and the carboxylic acid group of the N-carbamoyl-L-proline.

The main aim of the present work is to answer the following questions to reach a better understanding of the nature of these intramolecular processes: (a) Where and how do electron density changes take place throughout the reaction progress? (b) How can this rearrangement be related to chemical events such as the bond breaking/forming processes throughout the reaction progress? (c) How can these electronic reorganizations be described in detail? Or, in other words, what types of catastrophes and structural stability domains (SSDs) appear along each reaction pathway during the BET analysis?

2. Computational Background and Method

Following the Bader idea, Becke and Edgecombe have proposed the electron localization function (ELF), which measures the maximal probability for finding an electron pair

in a molecular species (molecule or crystal) [11]. The electron localization function (η) is defined by the following equation:

$$\eta\left(\vec{r}\right) = \frac{1}{1+\left(\frac{D_{\sigma(\vec{r})}}{D^0_\sigma\left(\vec{r}\right)}\right)^2} \tag{1}$$

where $D_\sigma\left(\vec{r}\right)$ and $D^0_\sigma\left(\vec{r}\right)$ are the electron localization for a real and homogenous gas, respectively, and their mathematical expressions are given by the Equations (2) and (3) in which, $\tau_\sigma\left(\vec{r}\right)$ corresponds to kinetic energy density while $\rho_\sigma\left(\vec{r}\right)$ defines electron density for a given σ spin.

$$D_\sigma\left(\vec{r}\right) = \tau_\sigma\left(\vec{r}\right) - \frac{1|\nabla\rho_\sigma|^2}{4\,\rho_\sigma\left(\vec{r}\right)} \tag{2}$$

$$D^0_\sigma\left(\vec{r}\right) = \frac{3}{5}\,(6\pi)^{2/3}\rho_\sigma{}^{5/3}\left(\vec{r}\right) \tag{3}$$

According to the Silvi–Savin approach [15,38] for a topological analysis, the electron localization function partitions the molecular space into different atomic basins. For that, two types of basins have been identified: core and valence basins. Valence basins, which are very important for a better description of chemical bond, are classified into monosynaptic basins [V(A)] and disynaptic basins [V(A,B)]. The first basin type is linked to lone pairs while the second is linked to shared electrons.

In order to evaluate the synchronicity of the chemical process along the different structural stability domains found in the BET analysis of the reaction pathway, we have defined in previous works [39,40] the synchronicity (S_y) index according to the following Equations (4)–(6), to be used when the number of SSDs is at least three:

$$S_y = 1 - \frac{2}{n(n-1)\left(S_f - S_0\right)} \sum_{i=1}^{n} \sum_{j=i+1}^{n} (S_j - S_i) \tag{4}$$

where n is the number of SSDs found along the BET analysis minus one, while S_f and S_0 are the final and initial IRC values, respectively. In Equation (4), S_j and S_i represent the values of IRC for the appearance of topological changes between SSDs. The maximum S_y value is 1 and its minimum value can be also determined by the following Equation (5):

$$S_y^{min} = 1 - \frac{2\left(\sum_{i=1}^{n}(n-i) - \sum_{i=1}^{n/2}(n-2i)\right)}{n(n-1)} \tag{5}$$

From Equations (4) and (5), the absolute synchronicity, S_y^{abs}, on a zero-to-one scale, is defined as:

$$S_y^{abs} = \frac{S_y - S_y^{min}}{1 - S_y^{min}} \tag{6}$$

The geometry of reactants, transition states and products were fully optimized using M06-2X [41] DFT functional together with cc-pVTZ basis set as implemented in Gaussian 16 [42]. The stationary points were characterized by frequency calculations in order to verify the number of imaginary frequencies (zero for local minima and one for transition states). In addition, the interconnectivity between the two minima (reactants and products) was verified by tracing the Intrinsic Reaction Coordinate (IRC) [43] curves within the second order Gonzalez–Schlegel integration method [44,45].

For the topological analysis within the BET theory, the wave function was extracted at each point of the IRCs and the ELF calculation was performed by means of the TopMod package [46] considering a cubic grid smaller than 0.2 bohr. This calculation renders the ELF

basins, either bonding, hydrogenated or non-bonding, as well as the electron population of each of the basins (i.e., of each of the bonds or lone pairs). We can then analyze the evolution of the population of those basins along the IRC and draw arrows representing the electron density flows. The basin population evolution along the IRC and the ELF isosurfaces of some chosen basins were visualized using Drawprofile and Drawmol [47,48].

3. Results and Discussion

3.1. BET Analysis along the Chemical Rearrangement of Allyloxycycloheptatriene Yielding Two Tricyclic Ketones

The chemical reaction yielding the formation of the tricyclic ketones **3** and **4** takes place via two steps, Scheme 1. The first one deals with the [3,3] sigmatropic rearrangement of allyloxycycloheptatriene, with formation of the intermediate **2**, while the second corresponds to the conversion of intermediate **2** into cycloadducts (tricyclic ketones) via an intramolecular Diels–Alder process (see also supplementary material).

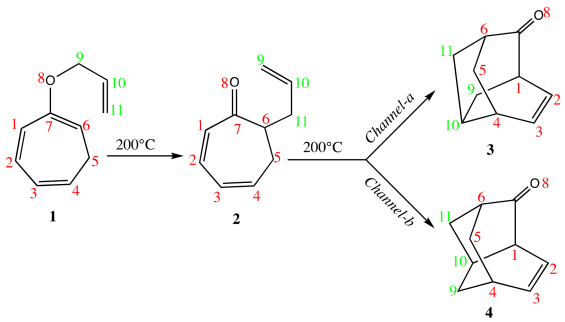

Scheme 1. Thermal sigmatropic rearrangement of allyloxycycloheptatriene to yield the tricyclic ketones **3** and **4**.

First Step: The BET Analysis along the [3,3] Sigmatropic Rearrangement of Allyloxycycloheptatriene.

Figure 1 displays the evolution along the IRC of the electron population of each basin engaged in the [3,3] sigmatropic rearrangement of allyloxycycloheptatriene according to the BET analysis. From this Figure, it can be seen that the procces of bond breaking (O8-C9) and forming (C6-C11) takes place along four SSDs. At the beginning of the first domain (distances d(O8-C9) = 1.427 Å and d(C6-C11) = 3.721 Å) the main basins (mono and disynaptic) are populated as follows: 3.52e for V(C6,C7), 1.42e for V(C7,O8), 4.97e for V(O8), 1.24e for V(O8,C9), 2.07e for V(C9,C10) and 3.44e for V(C10,C11), see Table S1 in the supporting information. It is worth noting that to avoid including non-significant data in the discussion, we will report the evolution along the IRCs of the total electron population of the set of basins accounting for each initial, final or transient double bond for all processes studied. Therefore, in the present case, the population reported as V(C10,C11) is the cumulated population of the basins appearing between C10 and C11 (two at the beginning of the process, one at the end) and the population reported as V(C9,C10) is also the cumulated population of the basins appearing between C9 and C10 (one at the beginning of the process, two at the end).

The transition between SSD-I and SSD-II (d(O8-C9) = 1.711 Å and d(C6-C11) = 2.167 Å) deals with the cleavage of an O8-C9 single chemical bond and the transfer of its electron population to an O8 lone pair. This cusp catastrophe allows increase of the population of V(O8) basin by 0.51e. In addition, the population of the V(C7,O8) basin slightly increases by 0.17e along SSD-I, and reaches 1.63e at the beginning of SSD-II. Along SSD-II, the population of the V(O8) basin records a loss of 0.34e and the populations of V(C9,C10) and V(C7,O8) increase by 0.26 and 0.14e, respectively.

The increase of the V(C7,O8) population continues along the third domain, SSD-III (d(O8-C9) = 1.857 Å and d(C6-C11) = 2.035 Å), illustrating the C7-O8 single to double

bond transformation. The same observation is noted for the V(C9,C10) basin. However, the main topological changes appearing along this domain correspond to the creation of two *pseudo-radical centers* [49] on C6 and C11 carbon atoms by means of two *fold-type* catastrophes. These two new monosynaptic basins [V(C6) and V(C11)] are populated with 0.41 and 0.28e at the beginning of the SSD-III domain, while the V(C6,C7) and V(C10,C11) disynaptic basins lose 0.42 and 0.52e, respectively.

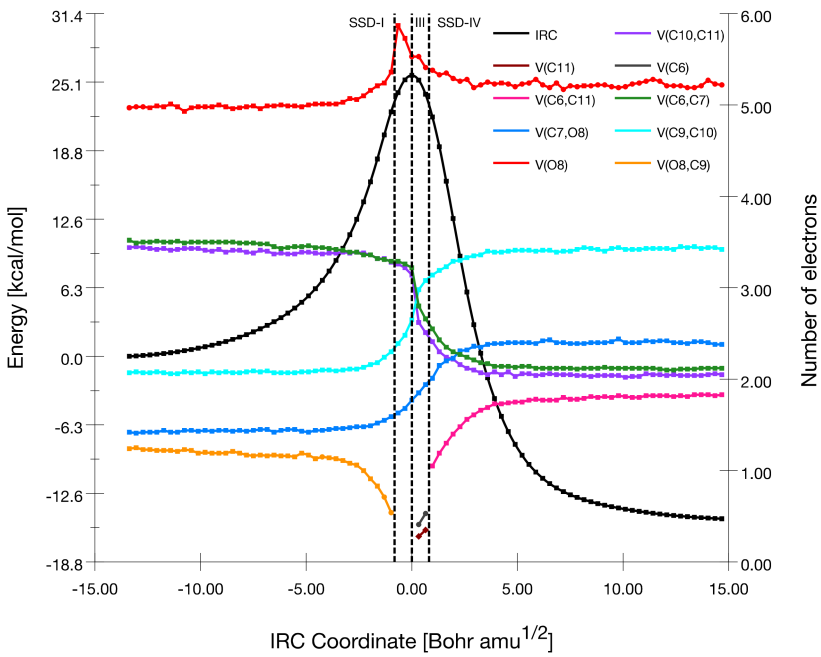

Figure 1. Population evolution (in e) of selected basins along the IRC associated with **TS1**.

Finally, at the beginning of the last domain, SSD-IV (d(O8-C9) = 1.949 Å and d(C6-C11) = 1.939 Å), the two new monosynaptic V(C6) and V(C11) basins disappear by combining together in order to form the disynaptic V(C6,C11) basin, which illustrates the formation of C6-C11 bond. The new V(C6,C11) basin holds a population of 1.05e and reaches 1.83e at the end of the domain. In parallel to that, we note also the total transformation of C7-O8 and C9-C10 single bonds into double ones (with of a total population of 2.38 and 3.42e for V(C7,O8) and V(C9,C10)) and the total depopulation of C6-C7 and C10-C11 double bonds into single ones, see also Figure 2.

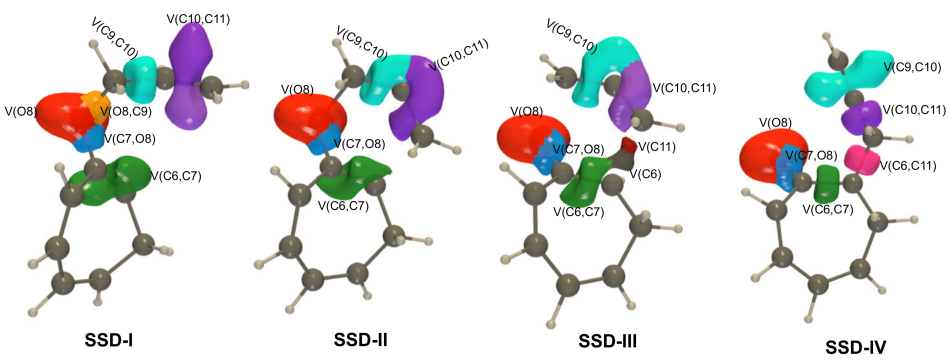

Figure 2. ELF basin isosurfaces (η = 0.7) of each of the SSDs found along the IRC associated with **TS1**. Color labeling of the basins is adopted according to Figure 1.

The main electron density motions can be schematically drawn as shown in Scheme 2, in which the disappearing basins (or in the case of double bonds, the basins losing a

significant part of their population) are red colored, while the appearing basins are green colored. The curly arrows stand for electron density flows and the large dots represent monosynaptic basins.

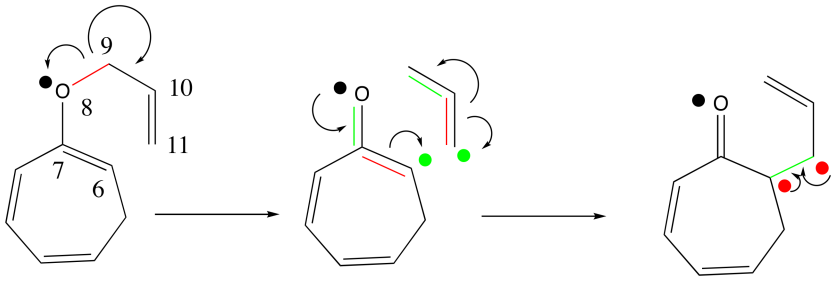

Scheme 2. Curly arrow representations of the main electron density flows of the reaction from **1** to **2**.

The IRC curve of **TS1** pathway starts at −13.37 Bohr amu$^{1/2}$ and ends at 14.67 Bohr amu$^{1/2}$, and the different SSDs appear at −0.65, 0.33 and 0.98 Bohr amu$^{1/2}$. With these values, the calculated S_y and S_y^{abs} are 0.96 and 0.94, respectively, thus indicating that the bond breaking/forming process takes place with a highly (94%) synchronous character.

Second Step: The BET Analysis along the Chemical Conversion of Intermediate 2 into the Tricyclic Ketones 3 and 4.

The second step deals with the conversion of intermediate **2** into tricyclic ketones that takes place via two channels: *fused* and *bridged*. For the *fused* (**TS2-a**) and *bridged* (**TS2-b**) channels, a series of five and four SSDs (Figures 3 and S1), respectively, are found along the corresponding IRCs.

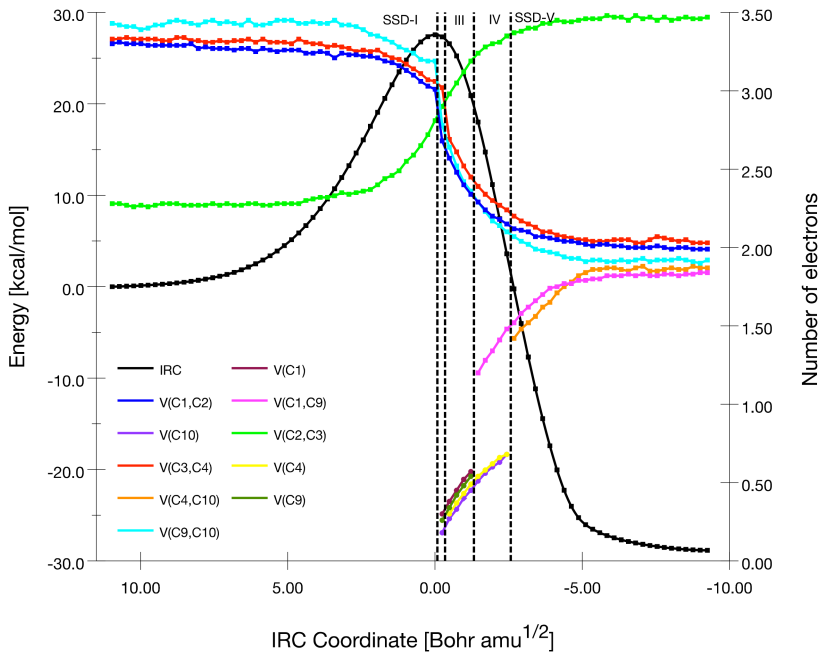

Figure 3. Population evolution (in e) of selected basins along the IRC associated with **TS2-a**.

For the *fused* channel yielding the species **3**, the first domain, SSD-I (initial distances, *d*(C1-C9) = 3.653 Å and *d*(C4-C10) = 3.115 Å), depicts the electron population of different atomic basins of intermediate **2** engaged in the formation of the new C-C chemical bonds, see Table S2. There are four main disynaptic basins describing the double bonds C1-C2 [V(C1,C2) with 3.30e], C3-C4 [V(C3,C4) with 3.33e] and C9-C10 [V(C9,C10) with 3.42e], and the single C2-C3 bond [V(C2,C3) with 2.28e]. At the end of the domain, some population changes are observed for different basins: V(C1,C2), V(C3,C4) and V(C9,C10) basins

experience a loss of 0.29e and 0.27e and 0.23e, respectively, while the V(C2,C3) electron population increases by 0.53e.

The electron population of V(C2,C3) continues increasing while V(C1,C2), V(C3,C4) and V(C9,C10) electron populations keep decreasing along the second domain SSD-II (initial distances, d(C1-C9) = 2.085 Å and d(C4-C10) = 2.327 Å). However, the main topological changes correspond to the appearance of three new monosynaptic basins (creation of three *fold-type F* catastrophes), V(C1), V(C9) and V(C10), integrating each one a population of 0.30, 0.18 and 0.26e, respectively. The electron population of these monosynaptic basins comes from the reduction in the populations of the disynaptic V(C1,C2) and V(C9,C10) basins.

The beginning of domain SSD-III (d(C1-C9) = 2.047 Å and d(C4-C10) = 2.296 Å) deals with the creation of a new monosynaptic basin V(C4) with a 0.34 electron population, corresponding to a *fold*-type catastrophe. Its population comes from the reduction in the population of disynaptic V(C3,C4). Furthermore, the electron population of the monosynaptic basins V(C1), V(C9) and V(C10) keep growing steadily and hit the pot at 0.57, 0.45, 0.54e, respectively, at the end of the domain.

The passage from the SSD-III domain to SSD-IV (d(C1-C9) = 1.898 Å and d(C4-C10) = 2.201 Å) describes the formation of the C1-C9 single bond with the transformation of C1-C2 and C9-C10 double bonds into single ones and which corresponds to the *cusp-type* catastrophe, Figure 4. The population of 1.20e for the new V(C1,C9) disynaptic basin comes from the disappearance of V(C1) and V(C9) monosynaptic basins.

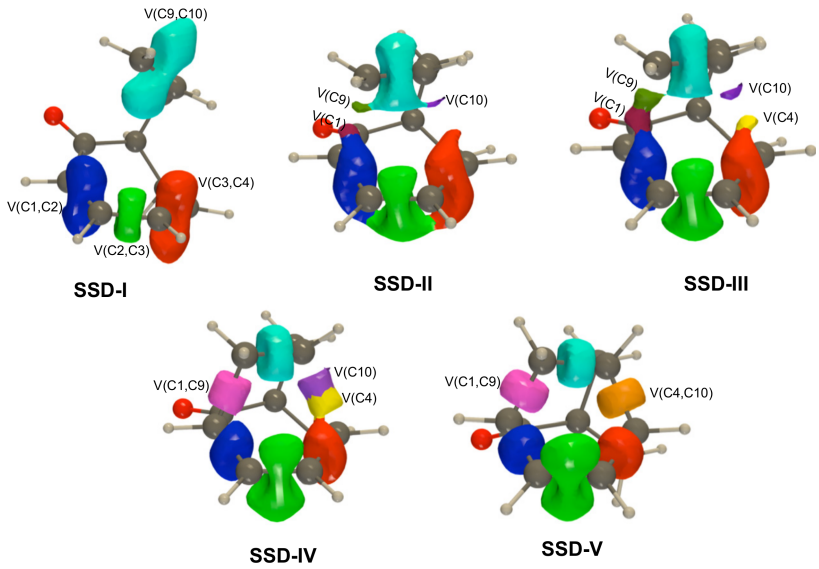

Figure 4. ELF basin isosurfaces (η = 0.7) of each of the SSDs found along the IRC associated with **TS2-a**. Color labeling of the basins is adopted according to Figure 3.

Finally, in the last domain [SSD-V (d(C1-C9) = 1.728 Å and d(C4-C10) = 1.989 Å)], the formation of the C4-C10 single bond takes place. The V(C4) and V(C10) basins disappear and their 0.68e population is transferred to the new V(C4,C10) basin, reflecting the creation of a C4-C10 bond, that appears with a population of 1.42e. The population of the new disynaptic basin V(C4,C10) reaches 1.87e at the end of domain.

The main electron density motions can also be schematically drawn using curly arrows, as shown in Scheme 3.

According to the reaction coordinates at which the different SSDs appear (−0.24, −0.48, −1.46 and −2.68 Bohr amu$^{1/2}$) along this reaction pathway, the calculated values of of S_y and S_y^{abs} are 0.98 and 0.96, respectively. The value of S_y^{abs} implies that the topological changes take place at 96% of the maximum absolute synchronicity, even higher than the preceding case.

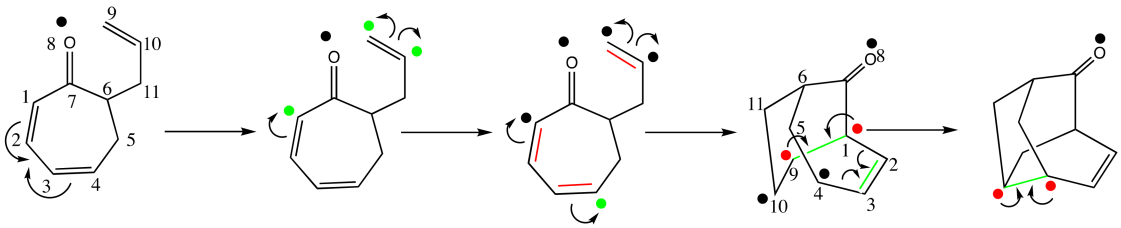

Scheme 3. Curly arrow representations of the main electron density flows o the reaction from **2** to **3**.

Similarly to the previous reaction channel (**TS2-a**), analysis of electron population of the selected basins engaged in the formation of new C4-C9 and C1-C10 single bonds along the *bridged* channel (**TS2-b**) are shown in Figure S1 and Table S3. Compared with the *fused* channel (**TS2-a**), BET results show that the bond forming process going through **TS-2b** is described by four stability structural domains (SSDs) instead of five. The main topological changes occur within domains SSD-II (appearance of monosynaptic basins on C4 and C9), III (appearance of monosynaptic basins on C1 and C10, and disappearance of the monosynaptic basins on C4 and C9 with concomitant appearance of the disynaptic V(C4,C9) basin), and IV (disappearance of the monosynaptic basins on C1 and C10 with concomitant formation of the disynaptic V(C1,C10) basin), Scheme 4 and Figure 5. The calculated S_y^{abs} is 0.90. Compared with the preceding analysis (S_y^{abs} = 0.96) the process of bond forming along this *bridged* channel is slightly less synchronous.

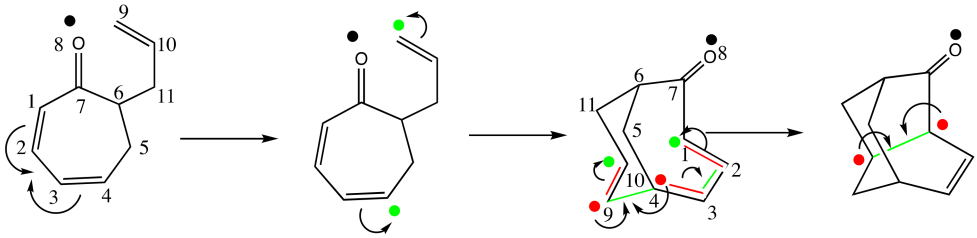

Scheme 4. Curly arrow representations of the main electron density flows of the reaction from **2** to **4**.

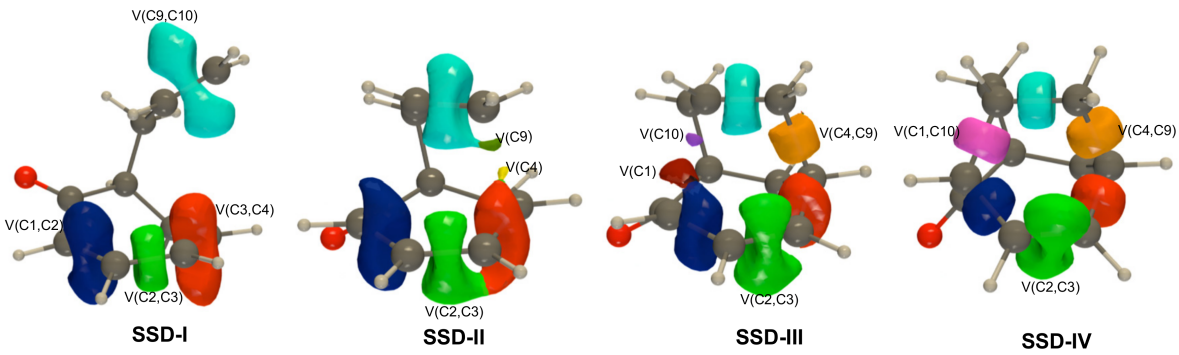

Figure 5. ELF basin isosurfaces (η = 0.7) of each of the SSDs found along the IRC associated with **TS2-b** Color labeling of the basins is adopted according to Figure S1.

3.2. Intramolecular Cycloaddition Reaction of Nitrone-Alkene 5

The mechanism of intramolecular 32CA of nitrone-alkene **5** takes place via two pathways (*fused* and *bridged*, Scheme 5), and for each channel we have carried out the BET analysis.

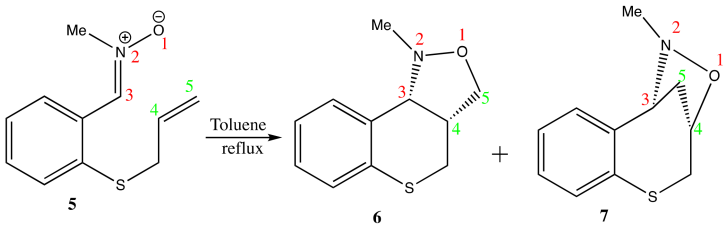

Scheme 5. Synthesis of tricyclic isoxazolidines from the nitrone-alkene **5**.

Along the *fused* channel (**TS3-a**) yielding the cycloadduct **6**, BET reveals that five SSDs are required for the description of the C3-C4 and O1-C5 forming bond processes, Figures 6 and 7. Along the first SSD-I (with initial distances *d*(C3-C4) = 2.977 Å and *d*(O1-C5) = 3.057 Å) a slight diminution in the V(O1,N2) basin population coupled with a slight increase in the V(N2,C3) population is sensed, see Table S4. The second domain (*d*(C3-C4) = 2.265 Å and *d*(O1-C5) = 2.024 Å) starts with a sudden decrease of the V(N2,C3) basin population due to the creation of a new V(N2) basin with a population of 1.12e (fold catastrophe) symbolizing the restoration of a lone pair on N2 nitrogen atom. Another two fold catastrophes, corresponding to the creation of V(C3) and V(C4) monosynaptic basins that take their population from the V(N2,C3) and V(C4,C5) disynaptic basins, respectively, occur at the beginning of the third domain (*d*(C3-C4) = 2.220 Å and *d*(O1-C5) = 1.976 Å).

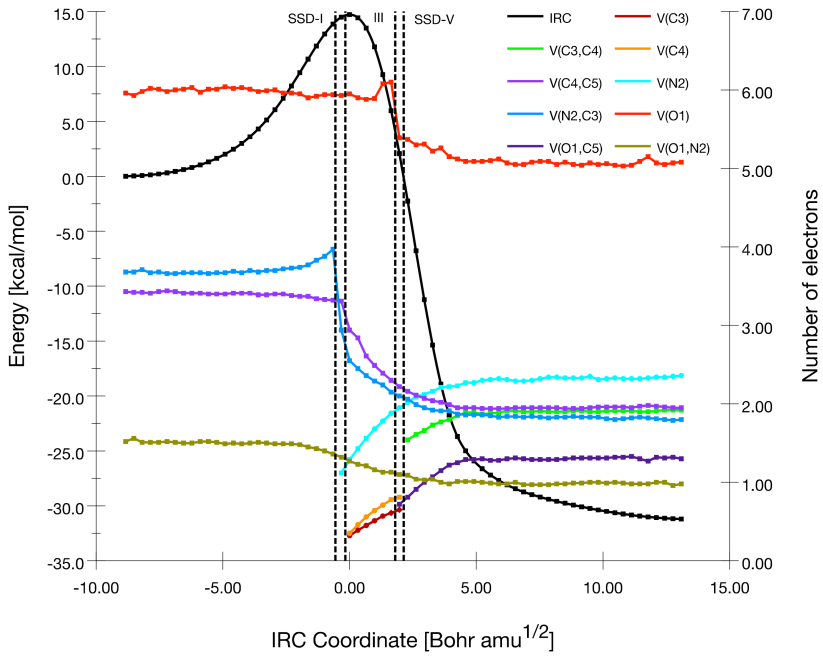

Figure 6. Population evolution (in e) of selected basins along the IRC associated with **TS3-a**.

These two catastrophes illustrate the creation of a *pseudo-radical center* on C3 [V(C3) with 0.35e] and C4 [V(C4) with 0.32e] carbon atoms, and which will be involved in the formation of the C-C bond. The fourth domain (*d*(C3-C4 = 1.941 Å and *d*(O1-C5) = 1.698 Å)) deals with creation of the V(O1,C5) disynaptic basin, which corresponds to the formation of the O1-C5 bond. Its population comes from the reduction in the population of V(O1), which records a drop of 0.71e. Finally, the fusion of the monosynaptic basins V(C3) and V(C4) happens at the beginning of the fifth domain (*d*(C3-C4 = 1.893 Å and *d*(O1-C5) = 1.653 Å)) with the creation of a new V(C3,C4) corresponding to the formation of C3-C4 bond. The new V(C3,C4) basin takes its population from the disappearance of the two former V(C3) and V(C4) monosynaptic basins present since the third domain. See Scheme 6 for a pictorial description of the electronic flows using curly arrows.

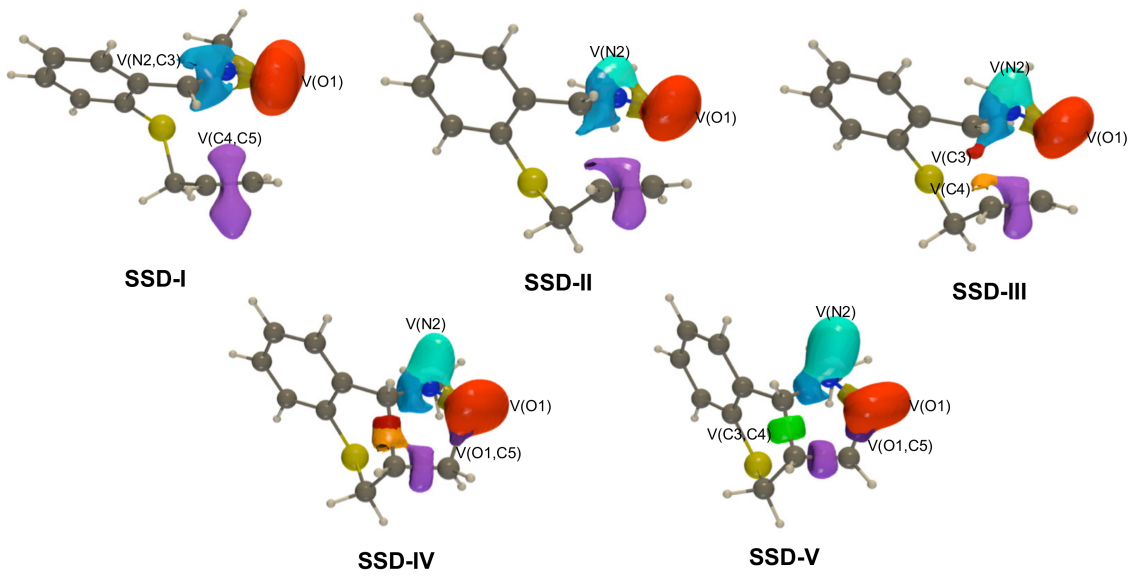

Figure 7. ELF basin isosurfaces (η = 0.7) of each of the SSDs found along the IRC associated with **TS3-a**. Color labeling of the basins is adopted according to Figure 6.

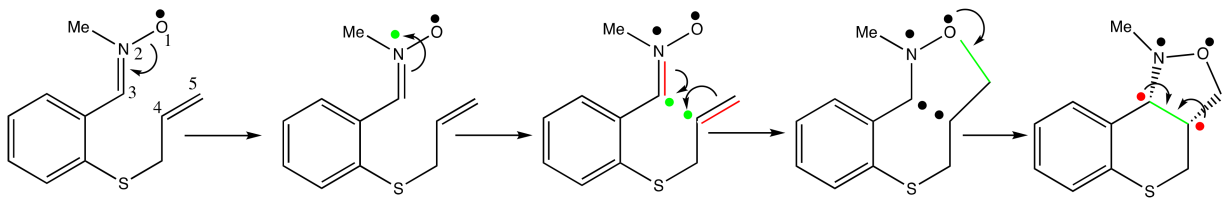

Scheme 6. Curly arrow representations of the main electron density flows of the reaction from **5** to **6**.

The different topological changes along this reaction pathway (varying from −8.88 to 13.09 Bohr amu$^{1/2}$) appear at the following reaction coordinates: −0.33, 0.0, 1.96 and 2.30, −0.27, −1.90 Bohr amu$^{1/2}$. By using these values, the corresponding values of S_y and S_y^{abs} are 0.93 and 0.89, respectively. The formation of new C-C and C-O bonds along **TS3-a** takes place with 89% synchronous character.

At variance with the *fused* channel, the process of forming new bonds along the *bridged* channel (**TS3-b**) is described by a series of seven SSDs, Figures 8 and S2, Scheme 7 and Table S5. The main difference comes from the creation of the pseudo-radical centers on C3 at SSD-III, and on C5 at SSD-IV, contrary to the *fused* channel where the monosynaptic basins responsible of the formation of the C-C bond (C3 and C4 on that case) have been created at the same domain (SSD-III). In addition, we note the transient creation of a monosynaptic basin V(C4), prior to the formation of the O-C bond. Similarly to the *fused* channel, the process begins with the creation of V(N2), but is followed in this case by the formation of the C3-C5 bond, while the appearance of V(O1,C4) finishes the process.

The different topological changes along this reaction pathway appear at the following reaction coordinates: 1.91, 1.09, 0.82, −0.27, −1.90 and −3.54 Bohr amu$^{1/2}$. By using these values, the corresponding values of S_y and S_y^{abs} are 0.93 and 0.88, respectively. The process takes place with 88% synchronous character, which is just 1% lower than the preceding analysis.

3.3. Thermal Decomposition of N-Carbamoyl-L-Proline

The decomposition of N-carbamoyl-L-proline takes place through two different reaction channels along **TS4-a** and **TS4-b**, corresponding to the dehydration and deamination processes, respectively (Scheme 8).

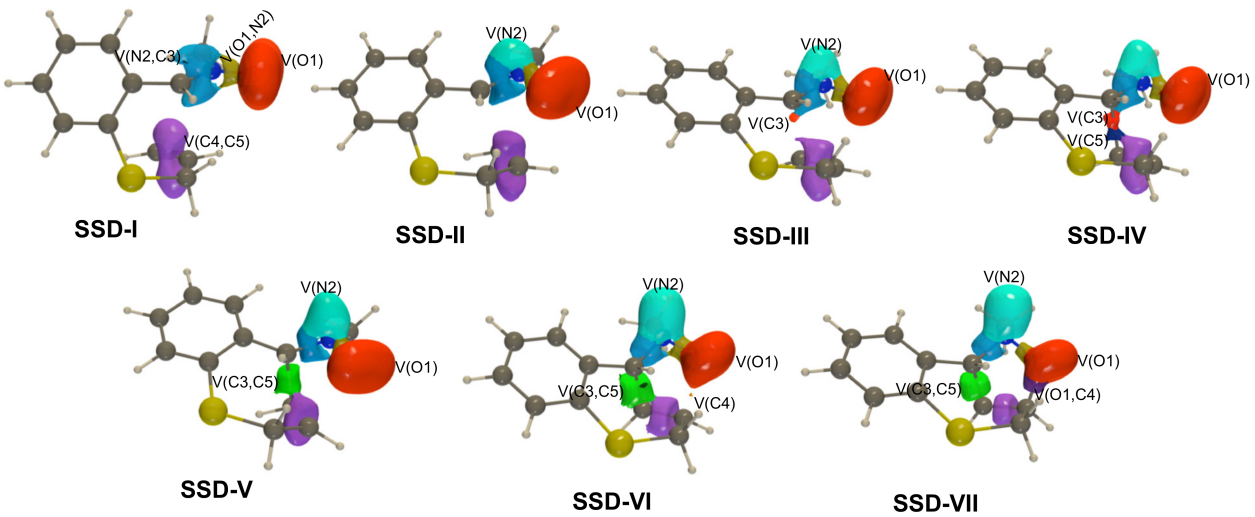

Figure 8. ELF basin isosurfaces (η = 0.7) of each of the SSDs found along the IRC associated with **TS3-b**. Color labeling of the basins is adopted according to Figure S2.

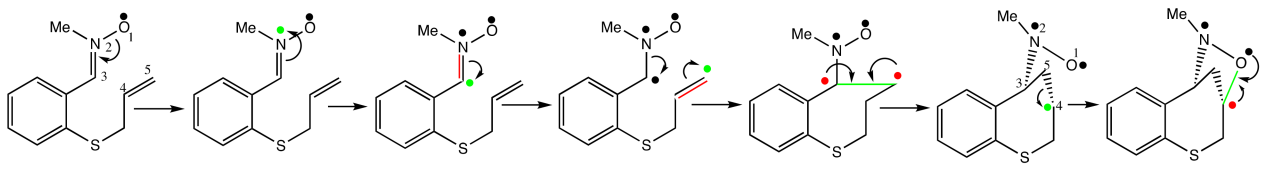

Scheme 7. Curly arrow representations of the main electron density flows of the reaction from **5** to **7**.

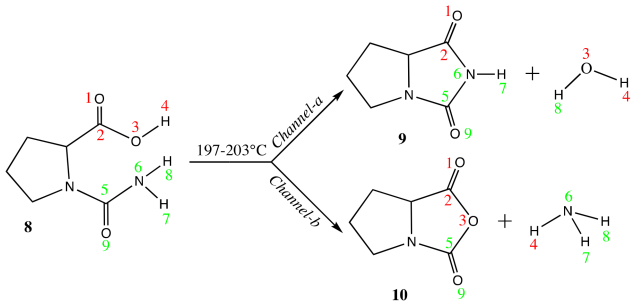

Scheme 8. Thermal decomposition of N-carbamoyl-L-proline.

For both reaction channels (water and ammonia elimination) five SSDs (see Figures 9–11 and S3, and Schemes 9 and 10) are found. The electron population evolutions of each basin engaged in the processes along the IRCs are reported in Tables S6 and S7.

For **TS4-a** (dehydration process), the transition from SSD-I (initial distances *d*(C2-N6) = 2.258 Å and *d*(O3-H8) = 2.311 Å) to SSD-II (*d*(C2-N6) = 1.886 Å and *d*(O3-H8) = 2.192 Å) deals with the disappearance of the V(N6) monosynaptic basin and the concomitant creation of the new C2-N6 bond as displayed in Figures 9 and 10 as well as in Scheme 9. This cusp catastrophe renders the appearance of the new chemical bond, and the initial population of the V(C2,N6) basin of 1.94e is mainly taken from the former V(N6) (which holds a population of 1.88e at the end of SSD-I). Along SSD-II the population of the V(C2,O3) basin records an important drop of 0.40e, which is mainly transferred to V(O3). At the beginning of SSD-III (*d*(C2-N6) = 1.647 Å and *d*(O3-H8) = 1.545 Å), the V(C2,O3) basin disappears, thus illustrating the cleavage of the C2-O3 bond (cusp catastrophe) and its population is transferred to the V(O3) basin. This population of V(O3) decreases along the rest of the process. At the beginning of SSD-IV (*d*(C2-N6) = 1.629 Å and *d*(O3-H8) = 1.163 Å) the main catastrophes recorded are the appearance of two new monosynaptic basins [V(N6)

with 1.85e and V(H8) with 0.36e] arising from the splitting of the former disynaptic basin V(N6,H8). The new V(N6) basin illustrates the restoration of the lone pair on the N6 nitrogen atom which was involved in the formation of the C2-N6 bond at the beginning of SSD-II. Finally, the V(H8) monosynaptic basin disappears at SSD-V with the formation of a new disynaptic basin, V(O3,H8), which represents the last topological change (formation of the O3-H8 single bond with a population of 1.86e). The population of V(O3,H8) comes from the reduction in the population of V(O3), which records a drop of 1.49e at the beginning of SSD-V (d(C2-N6) = 1.606 Å and d(O3-H8) = 1.061 Å), and also from the disappearance of V(H8).

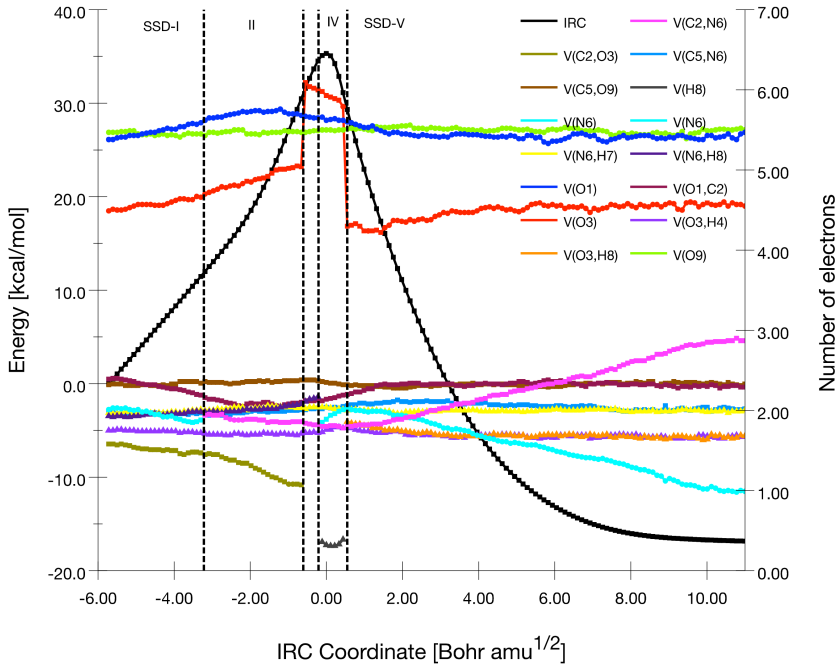

Figure 9. Population evolution (in e) of selected basins along the IRC associated with **TS4-a**.

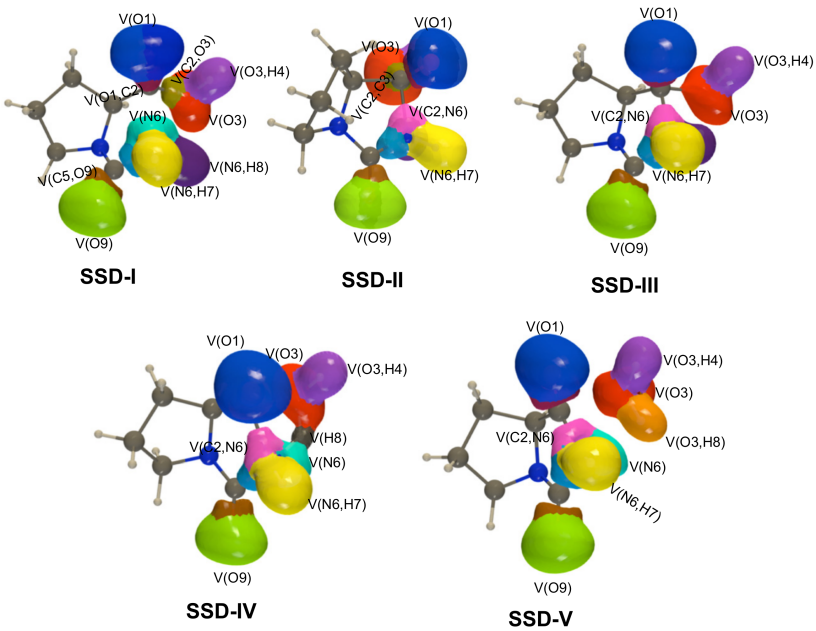

Figure 10. ELF basin isosurfaces (η = 0.7) of each of the SSDs found along the IRC associated with **TS4-a**. Color labeling of the basins is adopted according to Figure 9.

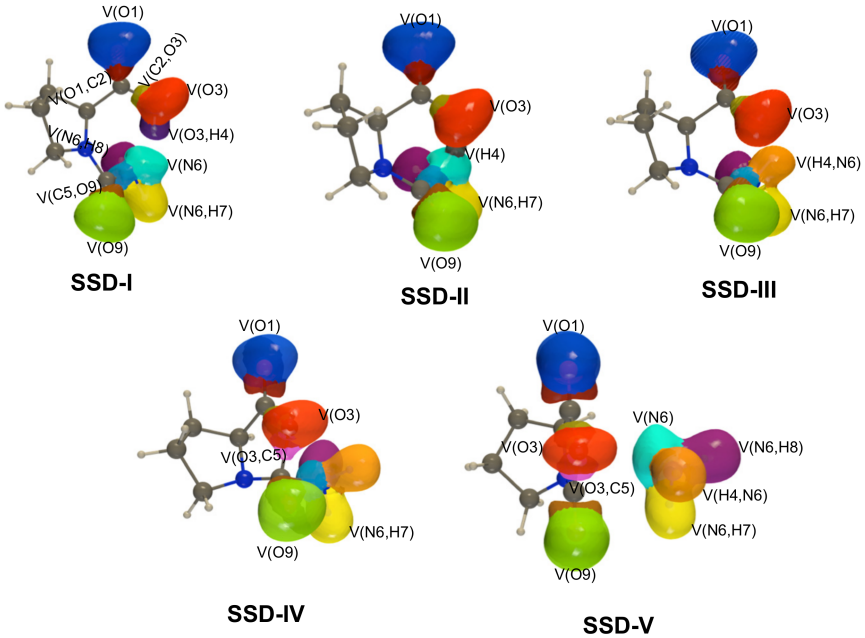

Figure 11. ELF basin isosurfaces (η = 0.7) of each of the SSDs found along the IRC associated with **TS4-b**. Color labeling of the basins is adopted according to Figure S3.

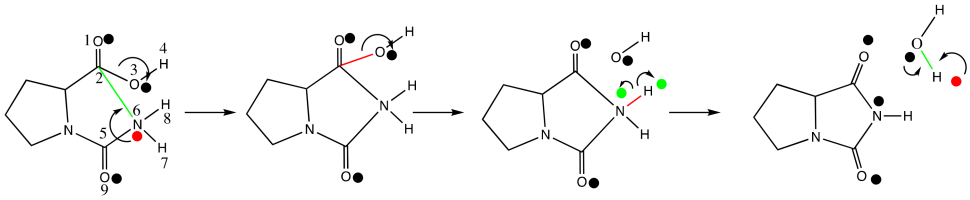

Scheme 9. Curly arrow representations of the main electron density flows of the reaction from **8** to **9**.

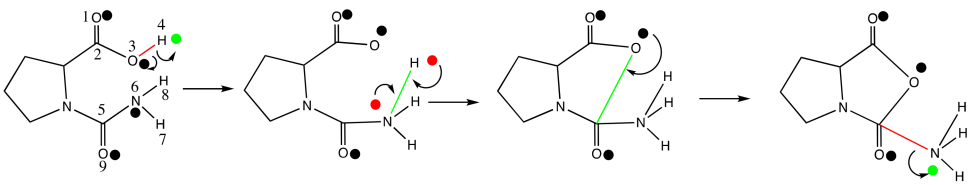

Scheme 10. Curly arrow representations of the main electron density flows of the reaction from **8** to **10**.

Along this reaction pathway, different topological changes (catastrophes) take place at the following reaction coordinates: −3.19, −0.55, −0.11 and 0.55 Bohr amu$^{1/2}$. Based on these coordinates, the calculated values of S_y and S_y^{abs} are 0.88 and 0.83, respectively. According to the S_y^{abs} value, the bond breaking/forming process along water elimination takes place with 83% synchronous character.

Concerning the deamination reaction process through **TS4-b**, the second SSD-II corresponds to the cleavage of O3-H4 with creation of V(H4) with 0.37e, Figures 11 and S3, Table S7 and Scheme 10. The remaining population of the former disynaptic basin V(O3,H4) is transferred to the V(O3) basin. The third SSD-III domain deals with the creation of the new bond, H4-N6, coming from the merging of two monosynaptic basins, V(H4) and V(N6). The creation of the new bond H4-N6 via the appearance of V(H4,N6) basin illustrates a cusp type catastrophe. Another catastrophe appears at the beginning of SSD-IV and represents the formation of the O3-C5 single bond, V(O3,C5) takes its population mainly from V(O3). At the last domain (SSD-V), the main topological change is the restoration of the monosynaptic V(N6) coming from the disappearance of the V(C5-N6) basin.

Like the previous reaction pathway, the corresponding reaction coordinates of different appeared topological changes are: −3.96, −3.26, 2.09 and 4.90 Bohr amu$^{1/2}$. The corresponding S_y^{abs} is 0.72 and implying a bond forming process along deamination reaction with 72% of synchronous character.

In Tables S8–S13 the energetic parameters of all stationary points found are collected, and the corresponding cartesian coordinates are also reported as supplementary materials.

4. Conclusions

The molecular mechanisms of three intramolecular reactions (the rearrangement of allyloxycycloheptatriene, I, the cycloaddition of a nitrone-alkene, II, and the decomposition of N-carbamoyl-L-proline, III) have been studied by means of BET, revealing that each reaction studied presents its own peculiarity for bond breaking and forming processes. The rearrangement I takes place in two steps, in which a series of four SSDs were observed during the first step. The process begins with the cleavage of the O8-C9 bond and the transfer of its electron population to the O8 lone pair, continues with the creation of two *pseudo-radical centers* on C6 and C11 carbon atoms and the first step finishes with the formation of the C6-C11 bond from the V(C6) and V(C11) monosynaptic basins. Considering the second step related to the conversion of intermediate **2** into tricyclic ketones, two reaction channels via *fused* (**TS2-a**) and *bridged* (**TS2-b**) transition structures are possible. For both channels, the main topological changes take place at the initial domains involving the creation of monosynaptic basins through *fold-type F* catastrophes (V(C1), V(C4), V(C9) and V(C10)), while the two new C-C bonds appear along the last two domains.

BET analysis of the rearrangements for II, reveals the presence of five SSDs describing the new C-C and O-C bond formation processes for the *fused* channel, while seven SSDs are needed to describe the *bridged* one. The main difference between the two channels comes from the creation of pseudo-radical centers on C3 and C5 in consecutive SSDs along the *bridged* case, in contrast with the *fused* one, where they appear on C3 and C4 in the same domain. In addition, we note the transient creation of a monosynaptic basin, V(C4), prior to the formation of the O-C bond in the *bridged* case, while in the *fused* case the equivalent V(C5) basin does not appear. In both paths, the process begins with the creation of V(N2). In the *fused* case, it follows the formation of the O-C bond and the C-C bond formation finishes the process, while in the *bridged* case the C-C bond is formed before the O-C one. It is worth noting that the *fused* channel has been found to be greatly favored from both a kinetic as well as a thermodynamic point of view in comparison with the *bridged* one.

Finally, according to BET analysis, the bond breaking and forming processes along the rearrangements III take place within five SSDs. For the water elimination pathway, the first two domains illustrate the formation of a C-N bond and the breaking of a C-O one with formation of hydroxide ion. The two last domains deal with the restoration of a N nitrogen lone pair and the creation of a new O-H bond via the cleavage of an H-N bond. For the deamination process, a different order of appearance for catastrophes is observed, with the cleavage of the H-O bond followed by the formation of the H-N bond, the formation of the new C-O bond and the breaking of the C-N bond with restoration of the N lone pair.

Supplementary Materials: The following supporting information can be downloaded at: https://www.mdpi.com/article/10.3390/physchem2030015/s1, Figure S1: Population evolution (in e) of selected basins along the IRC associated with **TS2-b**; Figure S2: Population evolution (in e) of selected basins along the IRC associated with **TS3-b**; Figure S3: Population evolution (in e) of selected basins along the IRC associated with **TS4-b**; Table S1: Basin Populations (in e), IRC coordinates (RX, amu1/2. Bohr) and C6-C11/O8-C9 chemical bonds (in Å) along the **TS1** reaction pathway; Table S2: Basin Populations (in e), IRC coordinates (RX, amu1/2. Bohr) and C1-C9/C4-C10 chemical bonds (in Å) along the **TS2-a** reaction path; Table S3: Basin Populations (in e), IRC coordinates (RX, amu1/2. Bohr) and C1-C10/C4-C9 chemical bonds (in Å) along the **TS2-b** reaction path; Table S4: Basin Populations (in e), IRC coordinates (RX, amu1/2. Bohr) and C3-C4/O1-C5 chemical bonds (in Å) along the **TS3-a** reaction path; Table S5: Basin Populations (in e), IRC coordinates (RX, amu1/2. Bohr) and C3-C5/O1-C4 chemical bonds (in Å) along the **TS3-b** reaction path; Table S6: Basin

Populations (in e), IRC coordinates (RX, amu1/2. Bohr) and C2-N6/O3-H8 chemical bonds (in Å) along the **TS4-a** reaction path; Table S7: Basin Populations (in e), IRC coordinates (RX, amu1/2. Bohr) and O3-C5/N6-H4 chemical bonds (in Å) along the **TS4-b** reaction path; Table S8: Relative electronic energies (ΔE, kcal/mol), enthalpies (ΔH, kcal/mol), entropies (ΔS, cal/mol.K) and Gibbs free energies (ΔG, kcal/mol) of activation and reaction for the thermal sigmatropic rearrangement of allyloxycycloheptatriene; Table S9: Electronic energies, enthalpies, entropies and Gibbs free energies (in a.u) of all species involved in the thermal sigmatropic rearrangement of allyloxycycloheptatriene; Table S10. Relative electronic energies (ΔE, kcal/mol), enthalpies (ΔH°, kcal/mol), entropies (ΔS°, cal/mol.K) and Gibbs free energies (ΔG°, kcal/mol) of activation and reaction for the IM32CA of nitrone-alkene 5; Table S11: Electronic energies, enthalpies, entropies and Gibbs free energies (in a.u) of all species involved in the IM32CA of nitrone-alkene 5; Table S12: Relative electronic energies (ΔE, kcal/mol), enthalpies (ΔH, kcal/mol), entropies (ΔS, cal/mol.K) and Gibbs free energies (ΔG, kcal/mol) of activation and reaction for the Thermal decomposition of N-carbamoyl-L-proline; Table S13: Electronic energies, enthalpies, entropies and Gibbs free energies (in a.u) of all species involved in the Thermal decomposition of N-carbamoyl-L-proline; cartesian coordinates.

Author Contributions: Investigation, A.I.A., J.A. and V.S.S.; Writing—original draft, A.I.A., J.A., M.O. and V.S.S.; Writing—review and editing, A.I.A., J.A., M.O. and V.S.S. All authors have read and agreed to the published version of the manuscript.

Funding: This research was funded by the Spanish Ministerio de Ciencia, Innovación y Universidades, grant number [PGC2018-094417-B-I00], by Generalitat Valenciana, grant number [AICO 2020/329], by Universitat Jaume I, grant number [UJI-B2019-30], by FNRS-FRFC, of the Walloon Region, and of the University of Namur (Conventions No. 2.5020.11, GEQ U.G006.15, 1610468, and RW/GEQ2016).

Institutional Review Board Statement: Not applicable.

Informed Consent Statement: Not applicable.

Data Availability Statement: Not applicable.

Acknowledgments: J.A., M.O. and V.S.S. thank financial support from the Spanish Ministerio de Ciencia, Innovación y Universidades for project PGC2018-094417-B-I00, from Generalitat Valenciana for project AICO 2020/329, and from Universitat Jaume I for project UJI-B2019-30. The calculations were performed on the computers of the Consortium des Equipements de Calcul Intensif (CECI) and particularly those of the Technological Platform of High-Performance Computing, for which the authors gratefully acknowledge the financial support of the FNRS-FRFC, of the Walloon Region, and of the University of Namur (Conventions No. 2.5020.11, GEQ U.G006.15, 1610468, and RW/GEQ2016).

Conflicts of Interest: The authors declare no conflict of interest.

References

1. Lewis, G.N. *Valence and the Structure of Atoms and Molecules*; The Chemical Catalog Company, Inc.: New York, NY, USA, 1923.
2. Pauling, L. *The Nature of the Chemical Bond, and the Structure of Molecules and Crystals*; Cornell University Press: Ithaca, NY, USA, 1960.
3. Lewis, G.N. The Atom and the Molecule. *J. Am. Chem. Soc.* **1916**, *38*, 762–785. [CrossRef]
4. Pauling, L. The Nature of the Chemical Bond. Application of Results Obtained from the Quantum Mechanics and from a Theory of Paramagnetic Susceptibility to the Structure. *J. Am. Chem. Soc.* **1931**, *53*, 1367–1400. [CrossRef]
5. Pauling, L. The Nature of the Chemical Bond. II. The One-Electron Bond and the Three-Electron Bond. *J. Am. Chem. Soc.* **1932**, *54*, 988–1003. [CrossRef]
6. Hehre, J.; Radom, L.; Schleyer, P.v.R.; Pople, J.A. *Ab Initio Molecular Orbital Theory*; John Wiley: New York, NY, USA, 1986.
7. Parr, R.; Yang, W. *Density-Functional Theory of Atoms and Molecules*; Oxford University Press: New York, NY, USA, 1989.
8. Geerlings, P.; De Proft, F.; Langenaeker, W. Conceptual Density Functional Theory. *Chem. Rev.* **2003**, *103*, 1793–1874. [CrossRef]
9. Bader, R.F.W.; Nguyen-Dang, T.T.; Tal, Y. Topological Theory of Molecular Structure. *Rep. Prog. Phys.* **1981**, *44*, 893. [CrossRef]
10. Bader, R.F.W. *Atoms in Molecules-A Quantum Theory*; Oxford University Press: Oxford, UK, 1990.
11. Becke, A.D.; Edgecombe, K.E. A Simple Measure of Electron Localization in Atomic and Molecular Systems. *J. Chem. Phys.* **1990**, *92*, 5397–5403. [CrossRef]
12. Kohout, M. A Measure of Electron Localizability. *Int. J. Quantum Chem.* **2004**, *97*, 651–658. [CrossRef]
13. Kohout, M.; Wagner, F.R.; Grin, Y. Electron Localizability Indicator for Correlated Wave functions. III: Singlet and Triplet Pairs. *Theor. Chem. Acc.* **2008**, *119*, 413–420. [CrossRef]

14. Thom, R. *Structural Stability and Morphogenesis, an Outline of a General Theory of Models*; Benjamin/Cummings Publishing Co.: Reading, MA, USA, 1980.
15. Silvi, B.; Savin, A. Classification of Chemical Bonds based on Topological Analysis of Electron Localization Functions. *Nature* **1994**, *371*, 683–686. [CrossRef]
16. Krokidis, X.; Noury, S.; Silvi, B. Characterization of Elementary Chemical Processes by Catastrophe Theory. *J. Phys. Chem. A* **1997**, *101*, 7277–7782. [CrossRef]
17. Adjieufack, A.I.; Liégeois, V.; Mbouombouo Ndassa, I.; Ketcha Mbadcam, J.; Champagne, B. Intramolecular [3 + 2] Cycloaddition Reactions of Unsaturated Nitrile Oxides. A Study from the Perspective of Bond Evolution Theory (BET). *J. Phys. Chem. A* **2018**, *122*, 7472–7481. [CrossRef]
18. Adjieufack, A.I.; Nouhou Nana, C.; Ketcha-Mbadcam, J.; Ndassa, I.M.; Andrés, J.; Oliva, M.; Safont, V.S. Deciphering the Curly Arrows Representation and Electron Flow for the 1,3-Dipolar Rearrangement between Acetonitrile Oxide and (1S,2R,4S)-2-Cyano-7-Oxabicyclo[2.2.1]Hept-5-en-2-yl Acetate Derivatives. *ACS Omega* **2020**, *5*, 22215–22225. [CrossRef]
19. Ríos-Gutiérrez, M.; Pérez, P.; Domingo, L.R. A Bonding Evolution Theory Study of the Mechanism of [3 + 2] Cycloaddition Reactions of Nitrones with Electron-Deficient Ethylenes. *RSC Adv.* **2015**, *5*, 58464–58477. [CrossRef]
20. Adjieufack, A.I.; Moto Ongagna, J.; Kenmogne Tchidjo, J.F.; Mbouombouo Ndassa, I. Topological Unveiling the [3 + 2] Cycloaddition Reaction between N-Methyl Phenyl Nitrone and Styrene Catalyzed by Chromium Tricarbonyl Complex from Electron Localization Function and Catastrophe Theory. *New J. Chem.* **2021**, *45*, 20342–20351. [CrossRef]
21. Cherni, E.; Adjieufack, A.I.; Champagne, B.; Abderrabba, M.; Ayadi, S.; Liégeois, V. Density Functional Theory Investigation of the Binding of ThioTEPA to Purine Bases: Thermodynamics and Bond Evolution Theory Analysis. *J. Phys. Chem. A* **2020**, *124*, 4068–4080. [CrossRef]
22. Viciano, I.; Gonzalez-Navarrete, P.; Andres, J.; Martí, S. Joint use of bonding evolution theory and QM/MM hybrid method for understanding the hydrogen abstraction mechanism via cytochrome P450 aromatase. *J. Chem. Theory Comput.* **2015**, *11*, 1470–1480. [CrossRef]
23. Mbah, M.B.; Adjieufack, A.I.; Nguimkeu, C.N.; Malloum, A.; Abode, A.; Zintchem, A.; Bebga, G.; Ndassa, I.M. Unraveling the Sequence of Electron Flow along the Cyclocondensation Reaction between Ciprofloxacin and Thiosemicarbazide through the Bonding Evolution Theory. *J. Mol. Graph.* 2022; *in press*. [CrossRef]
24. Chamorro, E.; Prado, Y.; Duque-Noreña, M.; Gutiérrez-Sánchez, N.; Rincón, E. Understanding the Sequence of the Electronic Flow along the HCN/CNH Isomerization within a Bonding Evolution Theory Quantum Topological Framework. *Theor. Chem. Acc.* **2019**, *138*, 60. [CrossRef]
25. Adjieufack, A.I.; Mbah Bake, M.; Nguemo Nguimkeu, C.; Pilmé, J.; Ndassa Mbouombouo, I. Exploring the Sequence of Electron Density Along the Chemical Reactions between Carbonyl Oxides and Ammonia/Water Using Bond Evolution Theory. *ChemPhysChem* **2021**, *22*, 1792–1801. [CrossRef]
26. Polo, V.; Gonzalez-Navarrete, P.; Silvi, B.; Andres, J. An Electron Localization Function and Catastrophe Theory Analysis on the Molecular Mechanism of Gas-Phase Identity S_N2 Reactions. *Theor. Chem. Acc.* **2008**, *120*, 341. [CrossRef]
27. Adjieufack, A.I.; Liégeois, V.; Mbouombouo Ndassa, I.; Champagne, B. Topological Investigation of the Reaction Mechanism of Glycerol Carbonate Decomposition by Bond Evolution Theory. *RSC Adv.* **2021**, *11*, 10083–10093. [CrossRef] [PubMed]
28. Safont, V.S.; Gonzalez-Navarrete, P.; Oliva, M.; Andrés, J. Inquiry of the Electron Density Transfers in Chemical Reactions: A Complete Reaction Path for the Denitrogenation Process of 2,3-Diazabicyclo[2.2.1]Hept-2-ene Derivatives. *Phys. Chem. Chem. Phys.* **2015**, *17*, 32358–32374. [CrossRef] [PubMed]
29. Gonzalez-Navarrete, P.; Andres, J.; Safont, V.S. A Bonding Evolution Analysis for the Thermal Claisen Rearrangement. An Experimental and Theoretical Exercise for Testing the Electron Density Flow. *Phys. Chem. Chem. Phys.* **2018**, *20*, 535–541. [CrossRef] [PubMed]
30. Zahedi, E.; Shaabani, S.; Shiroudi, A. Following the Molecular Mechanism of Decarbonylation of Unsaturated Cyclic Ketones Using Bonding Evolution Theory Coupled with NCI Analysis. *J. Phys. Chem. A* **2017**, *121*, 8504–8517. [CrossRef]
31. Andrés, J.; González-Navarrete, P.; Safont, V.S.; Silvi, B. Curly Arrows, Electron Flow, and Reaction Mechanisms from the Perspective of the Bonding Evolution Theory. *Phys. Chem. Chem. Phys.* **2017**, *19*, 29031–29046. [CrossRef]
32. Oliva, M.; Safont, V.S.; González-Navarrete, P.; Andrés, J. Electronic Structure and Rearrangements of Anionic $[ClMg(\eta^2\text{-}O_2C)]^-$ and $[ClMg(\eta^2\text{-}CO_2)]^-$ Complexes: A Quantum Chemical Topology Study. *Theor. Chem. Acc.* **2017**, *136*, 51. [CrossRef]
33. Andrés, J.; Safont, V.S.; Oliva, M.; Caster, K.L.; Goulay, F. A Bonding Evolution Theory Study of the Reaction between Methylidyne Radical, $CH(X^2\Pi)$, and Cyclopentadiene, C_5H_6. *Int. J. Quantum Chem.* **2022**, *122*, e26892. [CrossRef]
34. Cupas, C.A.; Kong, M.S.; Nullins, H.; Heyd, W.E. Multiple Thermal Rearrangements. III. The Pyrolysis of 7-(3-Butenyl)-Cycloheptatrie. *Tetrahedron Let.* **1971**, *34*, 3157–3160. [CrossRef]
35. Saubern, S.; Macdonald, J.M.; Ryan, J.H.; Woodgate, R.C.J.; Louie, T.S.; Fuchter, M.J.; White, J.M.; Holmes, A.B. Tricyclic-Isoxazolidine Analogues via Intramolecular 1,3-Dipolar Cycloaddition Reactions of Nitrones. *Tetrahedron* **2010**, *66*, 2761–2767. [CrossRef]
36. Chafaa, F.; Hellel, D.; Nacereddine, A.K.; Djerourou, A. A Theoretical Study of the Mechanism and Selectivity of the Intramolecular 1,3-Dipolar Cycloaddition Reaction of the Nitrone-Alkene derived from 2-Allylthiobenzaldehyde for the Synthesis of Tricyclic Isoxazolidines. *Tetrahedron Lett.* **2016**, *57*, 67–70. [CrossRef]

37. Seijas, L.E.; Mora, A.J.; Delgado, G.E.; Brunelli, M.; Fitch, A.N. Study of the conversion of N-carbamoyl-L-proline to hydantoin-L-proline using powder synchrotron X-ray diffraction. *Powder Diffr.* **2010**, *25*, 342–348. [CrossRef]
38. Silvi, B. The Synaptic Order: A Key Concept to Understand Multicenter Bonding. *J. Mol. Struct.* **2002**, *614*, 3–10. [CrossRef]
39. Adjieufack, A.I.; Mbouombouo Ndassa, I.; Patouossa, I.; Mbadcam, J.K.; Safont, V.S.; Oliva, M.; Andrés, J. On the Outside Looking in: Rethinking the Molecular Mechanism of 1,3-Dipolar Cycloadditions from the Perspective of Bonding Evolution Theory. The Reaction between Cyclic Nitrones and Ethyl Acrylate. *Phys. Chem. Chem. Phys.* **2017**, *19*, 18288–18302. [CrossRef]
40. Adjieufack, A.I.; Maraf Mbah, B.; Ketcha Madcap, J.; Mbouombouo Ndassa, I.; Andrés, J.; Oliva, M.; Safont, V.S. How Effectively Bonding Evolution Theory Retrieves and Visualizes Curly Arrows: The Cycloaddition Reaction of Cyclic Nitrones. *Int. J. Quantum Chem.* **2019**, *119*, e25985. [CrossRef]
41. Zhao, Y.; Truhlar, D.G. The M06 Suite of Density Functionals for Main Group Thermochemistry, Thermochemical Kinetics, Noncovalent Interactions, Excited States, and Transition Elements: Two New Functionals and Systematic Testing of Four M06-class Functionals and 12 Other Functionals. *Theor. Chem. Acc.* **2008**, *120*, 215–241.
42. Frisch, M.; Trucks, G.W.; Schlegel, H.B.; Scuseria, G.E.; Robb, M.A.; Cheeseman, J.R.; Scalmani, G.; Barone, V.; Mennucci, B.; Petersson, G.A.; et al. *Gaussian 16, Revision A. 03*; Gaussian Inc.: Wallingford, CT, USA, 2016.
43. Fukui, K. Formulation of the Reaction Coordinate. *J. Phys. Chem.* **1970**, *74*, 4161–4163. [CrossRef]
44. Gonzalez, C.; Schlegel, H.B. Reaction Path Following in Mass-Weighted Internal Coordinates. *J. Phys. Chem.* **1990**, *94*, 5523–5527. [CrossRef]
45. Gonzalez, C.; Schlegel, H.B. Improved Algorithms for Reaction Path Following: Higher-Order Implicit Algorithms. *J. Chem. Phys.* **1991**, *95*, 5853–5860. [CrossRef]
46. Noury, S.; Krokidis, X.; Fuster, F.; Silvi, B. Computational Tools for the Electron Localization Function Topological Analysis. *Comput. Chem.* **1999**, *23*, 597–604. [CrossRef]
47. Liégeois, V. DrawMol. UNamur. Available online: www.unamur.be/drawmol (accessed on 24 May 2022).
48. Liégeois, V. DrawProfile. UNamur. Available online: www.unamur.be/drawprofile (accessed on 24 May 2022).
49. Domingo, L.R.; Sáez, J.A. Understanding the Electronic Reorganization along the Nonpolar [3 + 2] Cycloaddition Reactions of Carbonyl Ylides. *J. Org. Chem.* **2011**, *76*, 373–379. [CrossRef]